Title: Multi-INT Signature Collection and Exploitation for Security:
Improving Discrimination, Analyses, and Passive Tracking Capabilities
for Time- and Distance-Varying Signatures in the Seismoacoustic Regime

Author(s):   Webster, Jeremy David; Carmichael, Joshua Daniel; Casleton, Emily
Michele; Schultz-Fellenz, Emily S.; Crawford, Brandon Michael; Coats,
Dane Erik; Collins, Adam Donald; Gard, Marvin Orrmond; Guiltinan, Eric
Joseph; Milazzo, Damien Michael; Pratt, Richard Dean; Swanson, Erika;
Begnaud, Michael Lee; Anderson, Dale

Intended for: Report

Issued: 2021-09-30

Multi-INT Signature Collection and Exploitation for Security:
Improving Discrimination, Analyses, and Passive Tracking Capabilities for Time- and
Distance-Varying Signatures in the Seismoacoustic Regime

Key Contributing Authors:
J. Webster[1], J. Carmichael[1], E. Casleton[2] and E. Schultz-Fellenz[3]

Project Team:
B. Crawford[3], D. Coats[3], A. Collins[3], M. Gard[3], E. Guiltinan[3], D. Milazzo[3], R. Pratt[3],
E. Swanson[3], M. Begnaud[1], D. Anderson[1]*

30 September 2021

[1] *Geophysics Group (EES-17), Earth and Environmental Sciences Division, LANL*
[2] *Statistical Sciences Group (CCS-6), Computer, Computational, and Statistical Sciences Division, LANL*
[3] *Earth Systems Observations Group (EES-14), Earth and Environmental Sciences Division, LANL*
* Project PI

1. Introduction and Project Summary

This project demonstrates the feasibility of a passive tracking capability for ground-based and airborne moving sources using multiple information streams from acoustic and seismic signals. These moving source types are characterized by their variability with time and distance (exemplified but not limited to the familiar doppler shift of a passing vehicle) and the signatures used for detection should have similar characteristics. We have demonstrated that time-varying sensor signatures (TVS) combined with time-stable sensor signatures provide a more complete understanding of moving source behavior. Importantly, we have collected a new, relevant LANL dataset of moving sources (small uncrewed aerial vehicle flights and ground vehicle movement), developed new signatures, and demonstrated the capability to identify, track and forecast the position of these moving sources.

The sensing modes for the effort included seismic and acoustic. We have leveraged the recent DDSTE-supported investment in rapid deployable sensors (the Los Alamos Rapid-deployable Sensor Array—LARSA), and uncrewed aerial vehicle (UAV)-based data collection systems and equipment. We identified suitable LANL locations and source types for the data acquisition.

The project was completed in three phases: 1) a well-planned field experiment at a testbed to provide data for signature construction, algorithm development, and ground truth collection for validation; 2) signature discovery–the mathematical development of features from the acoustic and seismic source signals; and 3) the demonstration of source/target tracking capability with the experimental data.

The experimental testbed is located on LANL property, in a portion of Technical Area 51 (TA-51) colloquially referred to as the Pinon-Juniper (P-J) plot, where plant physiological observations and measurements have been made regularly for many decades. The field experiment used ground-based rapid-deployable sensors to detect general operational activities of ground and low-altitude airborne equipment. The uncrewed aerial vehicle (UAV) flights executed at the TA-51 P-J plot replicated potential relevant signatures of different airborne flight profiles of interest. The determination of ground-based seismic and acoustic sensor deployment locations was performed using an approach from Bayesian design of experiment (DoE) [1,2] to optimize the usefulness of the expected signals from the selected source locations. A suite of target/source locations/paths were identified and used to inform the experimental design. Additionally a three element acoustic array was designed based on the expected acoustic signature of the UAV. This array was deployed near the center of the P-J plot and would provide data for traditional array beamforming algorithms to track the motion of the source vehicles.

One of the greatest challenges was the construction of signatures indicative of sources/targets movement. To overcome this difficulty, the team leveraged decades of research experience in underground source location. For fixed sources, a common approach is to identify segments of transient and continuous wave time series that isolate source information. An analogous approach was taken in this research for moving sources. Acoustic and seismic time series were discretized over time into small segments enabling application of fixed-source analysis methods for each segment.

Through this project, we demonstrated the ability to design and efficiently execute relevant field campaigns with in-situ sensor deployment and complex signature generation from ground-based and airborne sources. We have also demonstrated the capability to use three component seismic data to differentiate between ground-based moving sources, based on their speed. We have also demonstrated the capability to detect aerial vehicle signatures and track them using acoustic beamforming techniques. Lastly, we have applied a forecasting framework that will be able to predict the location of a moving source given its current position with uncertainty.

2. Sensors and Sources
a. LARSA (sensor)
This campaign served as the first significant test of the LARSA system. LARSA was designed to be a customizable, field-deployable sensor and data acquisition system with the ability to perform high frequency, multi-phenomena sensor measurements quickly and reliably. Since this study required field deployed digitizers and seismic and acoustic sensors with simultaneous sampling rates of at least 5 kHz, this was an ideal use case for the LARSA system.

For this measurement the digitizer was equipped with an acoustic/vibration data acquisition module which was configured to take data at 5120 samples per second, as well as a GPS module that provided accurate timestamps of the data.

The deployed microphones were GRAS 146AE ½" free field microphones. These are ruggedized research grade microphones that are waterproof and designed to survive shocks and extreme temperatures with no degradation in sensitivity.

The deployed seismic sensors were Geospace HS-1 geophones. These are compact, research grade instruments that measure velocity ground motion in three orthogonal directions (1 vertical and 2 horizontal), and have a low frequency cutoff at 2 Hz.

b.   Uncrewed Aerial Vehicle (airborne source)

For low-altitude aerial vehicle signature exploitation, LANL's Earth Systems Observations Group (EES-14) deployed one select aircraft in its UAV fleet for this experimental campaign. The deployed aircraft was a Gryphon Aether X8 heavy-lift-capable coaxial quadcopter (Figure 1). This aircraft has a dry weight of 12.7 kg, and is powered by four 12,000mAh lithium polymer batteries. While the aircraft is capable of achieving a total takeoff weight (aircraft + batteries + sensor(s)) of 35.8 kg, the qualifications of the team's pilots under the Federal Aviation Administration's (FAA) Part 107 small UAV piloting requirements limits the maximum takeoff weight to 24.9 kg. Its maximum forward speed is 20 m/s. For one mission, the aircraft carried a synthetic payload to simulate the signatures of a load-bearing flight mission, and for comparison against the signatures detected by LARSA of the payload-free aircraft.
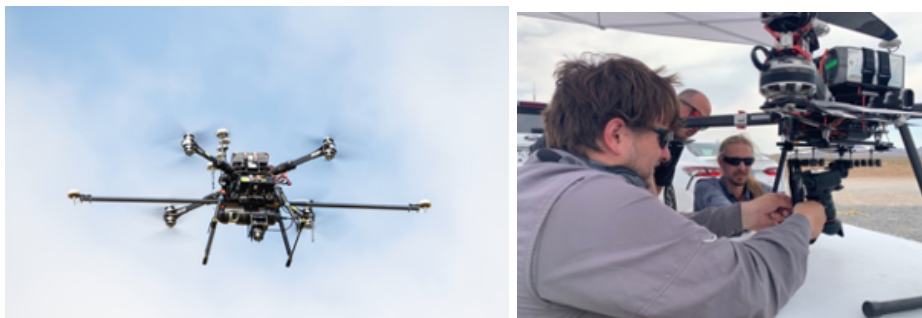
Figure 1. *(Left) Photo of the EES-14 Gryphon Aether X8 heavy-lift coaxial quadcopter in flight, configured for LIDAR deployment. (Right) LANL uncrewed aerial systems (UAS) team members affix an optical camera to the Gryphon's payload rails for data collection.*

The experienced UAV deployment team in LANL's EES-14 group has executed successful scientific R&D sensor deployment and data collection missions at various locations around the continental U.S. and Alaska since 2015. The LANL uncrewed aerial systems (UAS) team has a track record of operational excellence at other U.S. Government controlled sites, including the Nevada National Security Site, where the

team has performed flight operations and data collection in support of obtaining transient signature information for characterization of surface and subsurface explosions. This project provided an exciting opportunity for this team to operate their equipment as signature and not sensor, and to design a field campaign with realistic operational parameters for both surveillance and threat mission profiles.

### c. Ground Vehicle fleet (ground-based source)

In addition to the deployment of an airborne vehicle in different flight paths, the field campaign included deployment of a small fleet of different types of passenger vehicles traversing a dirt road encircling the TA-51 P-J plot. This provided another suite of data against which time- and distance-varying signature detection using seismic and acoustic data streams could be evaluated. The vehicles deployed for the field campaign included a 4x4 heavy-duty diesel pickup truck, a utility task vehicle (UTV), a small passenger vehicle, and a large SUV. The vehicles traversed the road at two different peak rates of speed and each had an onboard, portable handheld GPS unit to establish location and timing of signals. The field team recorded start times of each vehicle's transit around the dirt road for signature verification. Terrestrial vehicle signatures were recorded when the UAV was not in the air, to reduce complexity in multi-signature discrimination.

3. Statistical Analysis for Sensor Deployment Optimization

Sensors were placed by considering the optimal location for answering a question of interest, specifically, "where is the UAV?". A priori, we did not expect a significant seismic signature, so the sensor placement was optimized on the predicted acoustic signal. Because the TA-51 P-J plot is a small area, we can assume that the atmosphere is consistent and that acoustic waves will travel at the same rate from the UAV to the LARSA sensor, regardless of the location of either. Therefore, the full Bayes DoE optimization technique, as performed in other deployment scenarios (e.g., for seismic in [3]), is not necessary. Instead, we only need to consider the distance from the sensor to the path of the UAV, with the goal of minimizing the cumulative distance over the entire flight.

Figure 2 demonstrates this methodology. The colored region represents the 13,015 possible sensor locations, which are colored by their distance from the UAV integrated over the entire flight path (gray dashed lines). We expect the UAV to be louder, and thus produce a stronger acoustic signal, at the launch/land site (gray box) and as it rounds the corners (gray stars) since those areas are co-located at points where the UAV will be experiencing the most change in motor performance (to climb/descend and to make turns, respectively), thus prioritizing placing sensors near these sites. In addition to considering the expected acoustic sound at each location, it is also important to space the sensors to produce coverage of the area. Thus, for all those points with cumulative distance below a threshold, a space-filling design was used to determine the final sensor locations. This design employs a maxi-min approach, which adds new sensors sequentially by maximizing the minimum distance between all existing sensors. The resulting sensor locations are shown as black circles in Figure 2.
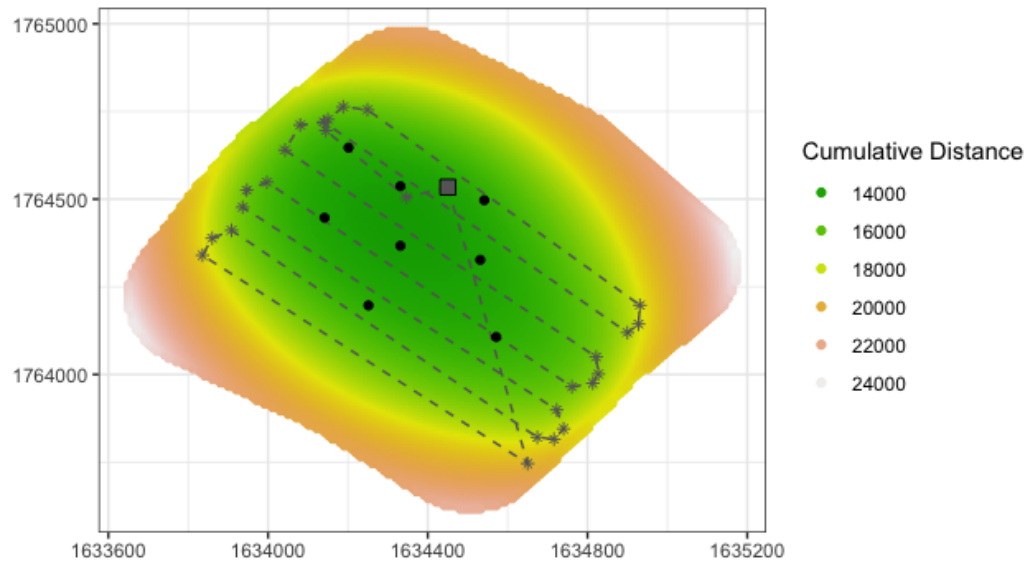
Figure 2. Demonstration of optimal sensor deployment. Colored points represent the 13,015 possible sensor locations colored according to the cumulative distance from points of interest on the UAV flight (dashed line). Gray box represents the launch/land site and gray stars indicate the points where the UAV turns a corner, both of which we expect to make a larger acoustic signal. Black circles represent the eight optimal sensor locations.

4. Field Campaign
a. LARSA deployment
In all, ten LARSA stations were deployed in the TA-51 P-J plot (Figure 3). Eight of the stations were located at positions determined by the statistical sensor deployment optimization method described in Section 3a (Figure 2), and two (numbers 122 and 127 in the figure below) were located at larger distances from the flight paths in order to test the range of the acoustic and seismic sensors. Each of the stations had a Geospace HS-1 three component geophone installed along with a GRAS 146AE 1/2" CCP Free-field Microphone. One site (number 120) had a small acoustic array installed. This array consisted of three of the GRAS microphones deployed in an equilateral triangle approximately 0.5 m on each side. GPS positions of each element were taken with a survey-grade differential GPS unit for approximately 1 cm accuracy.

Figure 3. Image showing the deployed locations of the 10 LARSA stations (orange triangles) at the TA-51 Pinon-Juniper (P-J) plot. The P-J plot is roughly bounded by the rounded rectangular dirt road, Leonard Lane Loop, at the center of the image.

b. Low-altitude aerial deployment (UAV flights)

Prior to the initiation of field operations, the flight team assembled the UAV aircraft in a nearby laboratory and transported it to the launch-land point by vehicle. The aircraft was initially deployed in a payload-free configuration, and operated in that manner for most missions.

While in-field flight checks were in process at the launch/land site, the flight team uploaded the pre-configured flight profiles to the flight controller. This ensured at least partial autonomous operation of the UAV for some of the missions.

Seven flight missions were designed following two principal flight profiles - surveillance and threat. The two types of surveillance flight profiles (Figure 4) involved the aircraft following an oblique circular pattern for perimeter surveillance, and a pre-designed boustrophedonic flight pattern, which maintained a constant altitude, heading, and forward speed throughout the duration of the mission. The boustrophedonic flight mission is most similar to missions previously executed by this team for other customers [4,5,6]. The field campaign included a total of four surveillance missions, two each at 35 m and 50 m AGL, and all at a vehicle forward speed of 3 m/s.
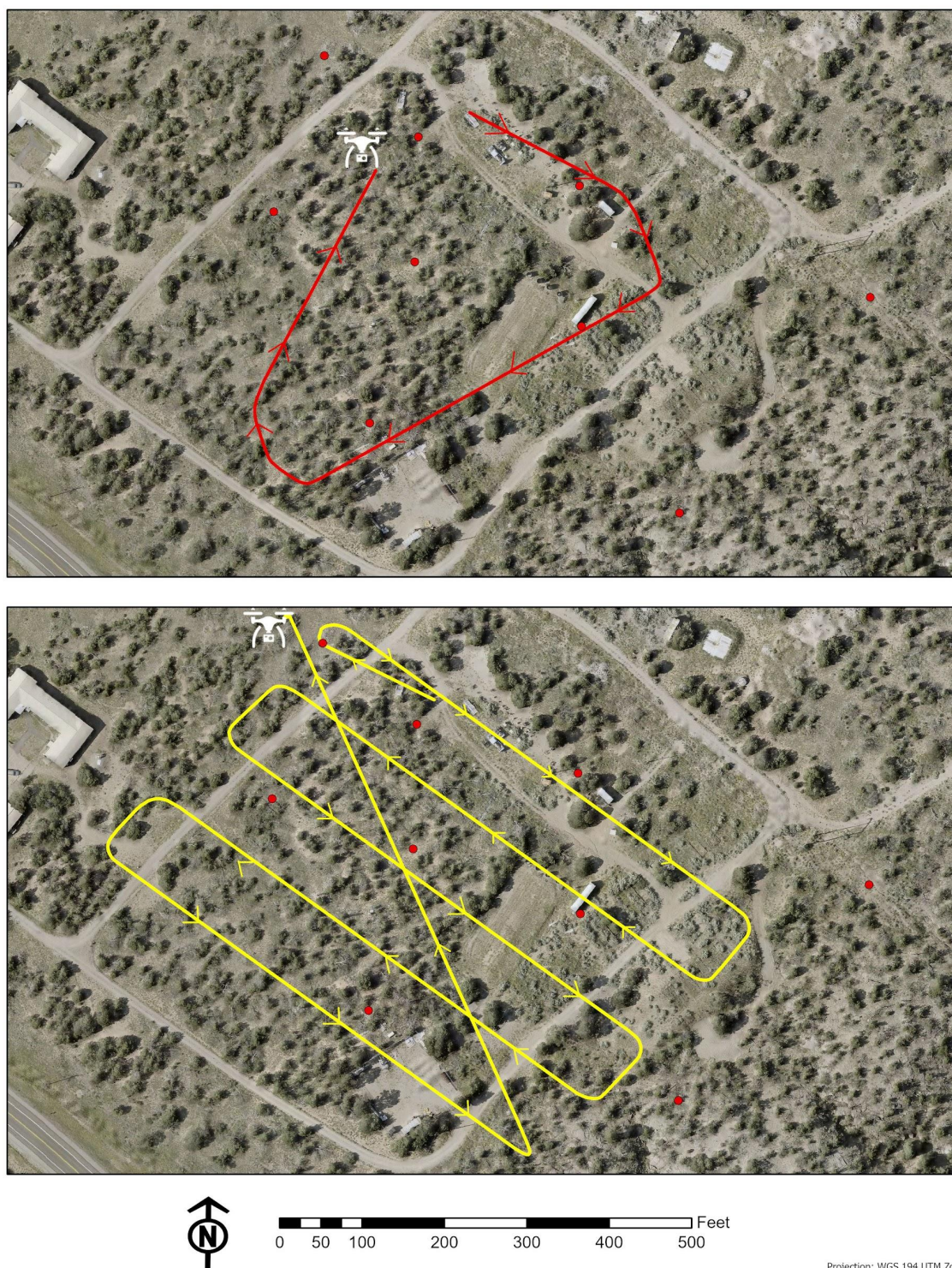
6

Figure 4. *Two types of surveillance flight profiles flown during the field campaign. (Upper) Perimeter surveillance pattern shown in red. (Lower) Boustrophedonic surveillance pattern shown in yellow. Arrows indicate direction of travel of the UAV from the launch point. Both surveillance flight profiles were flown at 35 m AGL and 50 m AGL over the same path. Red dots indicate the position of the LARSA sensors.*

Five threat-oriented missions were flown in the field campaign (Figure 5), whose flight plans were informed by relevant stakeholders at LANL (G. Andy Erickson, GS-PROG; Don 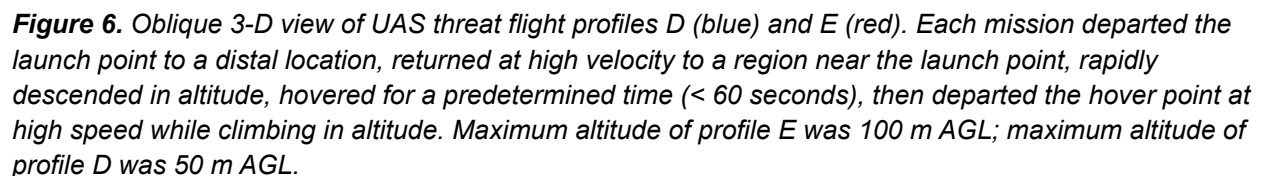O'Sullivan, GS-NSD; and Julian Atencio, SEC-DO). All threat profiles involved the aircraft traveling at varying altitudes and speeds, up to a maximum vehicle forward speed of 15 m/s.
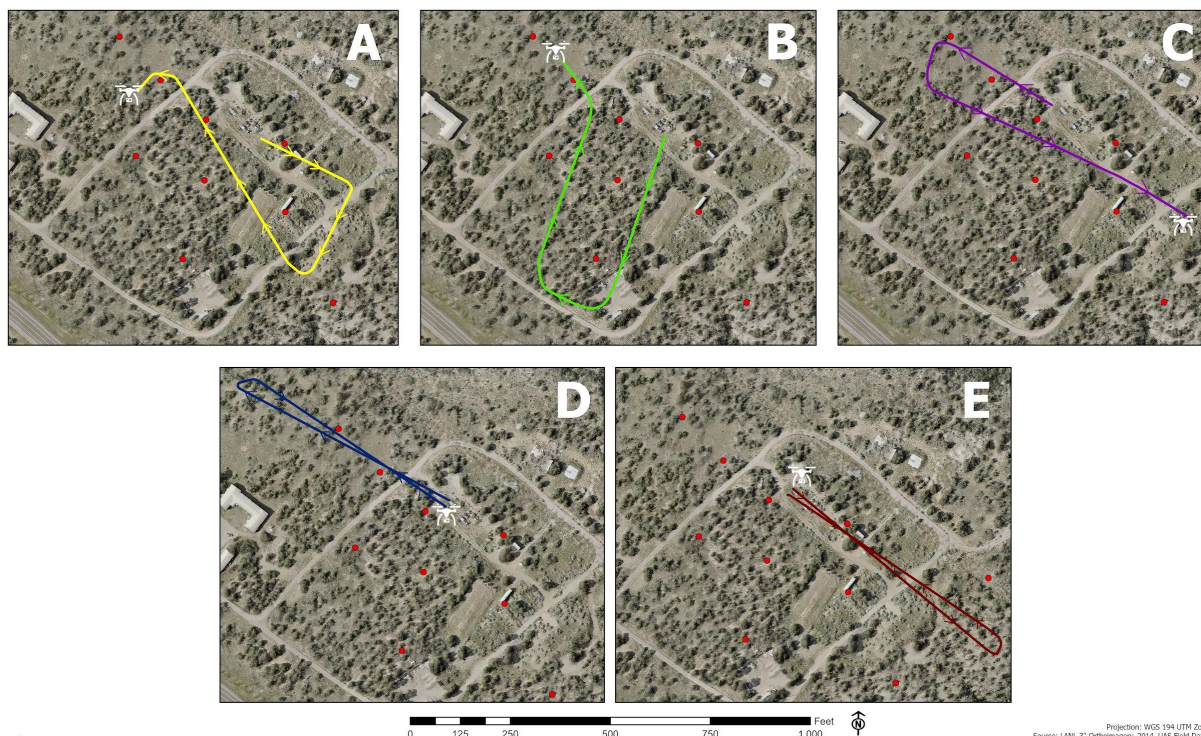
Figure 5. *Maps showing the five threat-oriented flight profiles flown during the campaign. A (yellow), B (green), and C (purple) were designed and flown in an aggressive attack style, while D (blue) and E (red) were designed and flown for exfiltration purposes. See text for further discussion and Figure 6 for additional detail on the D and E flight missions' vertical profiles.*

The five threat missions can be subdivided into two general profiles - aggressive attack and exfiltration. The three aggressive-attack-style threat profiles were designed with the aircraft initially positioned at a distal location, then approaching the target at maximum speed and stopping rapidly (mimicking a collision or crash). The exfiltration-style threat profile involved the aircraft approaching a target location at high velocity from two different positions and altitudes, rapidly decreasing in altitude at the target location to < 5 m AGL, hovering for 15-60 seconds, then departing the hover site at a high rate of speed while simultaneously climbing in altitude (mimicking an approach to a location, collecting or releasing a payload, then fleeing the site) (Figure 6).

Figure 6. *Oblique 3-D view of UAS threat flight profiles D (blue) and E (red). Each mission departed the launch point to a distal location, returned at high velocity to a region near the launch point, rapidly descended in altitude, hovered for a predetermined time (< 60 seconds), then departed the hover point at high speed while climbing in altitude. Maximum altitude of profile E was 100 m AGL; maximum altitude of profile D was 50 m AGL.*

The team executing UAS operations and analyses for this campaign was as follows:

- Damien Milazzo, EES-14, mission command pilot;
- Adam Collins, EES-14, mission command pilot;
- Eric Guiltinan, EES-14, backup pilot and data analyses;
- Brandon Crawford, EES-14, backup pilot, GPS surveying, and data analyses;
- Erika Swanson, EES-14, mission planning and flight telemetry;
- Dane Coats, EES-14, GPS surveying, field support, and data analyses;
- Richard Pratt, EES-14, geospatial analyses and cartographic production.

The UAS fielding team, including the pilot cadre, includes technical subject matter experts in geoscience, structural geology, geospatial analysis, computational modeling, plant physiological ecology, radiation detection, and machine learning. Having a deployment team who are scientific and technical SMEs first provides a

9

foundational capability for campaign design focused on maximized technical objectives, effectiveness and efficiency; staff that can successfully execute those campaigns, and the same team also provides physics-informed data analyses and interpretation to customers.

c. Ground-based vehicle deployment

Four vehicles were utilized for the ground-based vehicle tracking portion of the measurements, including a Ford F250 heavy-duty pickup truck, a John Deere Gator UTV, a Toyota Corolla small passenger vehicle, and a Chevy Tahoe large SUV (no GPS data available from the Chevy Tahoe). Most vehicles were equipped with a handheld GPS recorder to track its position as a function of time. Each vehicle was driven twice around the Leonard Lane Loop surrounding the TA-51 P-J plot (Figure 3). For all vehicles, its first lap was completed at a slower speed (approximately 10 mph) and the second lap was completed at a higher speed (approximately 20 mph). Ground vehicle transits did not take place contemporaneously with airborne UAV flight operations.

d. Opportunistic natural earthquake signature detection

The LARSA-UAV field campaign was initially attempted on 30 June 2021. On that date, LARSA was fully deployed, but airborne operations were severely limited due to inclement weather. Two abbreviated surveillance flight missions were executed on 30 June; one was conducted payload-free and another was performed with the aircraft carrying payload. Since not all flight missions were able to be executed on that date, the campaign was rescheduled to 12 July. LARSA was demobilized on 1 July and returned to their storage facility for data download and maintenance.

On 12 July 2021, the team redeployed the LARSA sensors and tested their operation prior to 09:00 local time. As the team was preparing for airborne operations, some members of the field team identified abrupt but gentle, brief shaking similar to that of an earthquake. Immediate outreach to the operating technical staff of the Los Alamos Seismic Network (LASN) identified that at around 09:35 local time, a magnitude 4.2 mainshock earthquake occurred near the intersection of the Nacimiento and Gallina faults northwest of Los Alamos (Figure 7). Further analyses showed four earthquakes associated with this event: a mainshock, a foreshock and two aftershocks. LASN analyses showed these events were all magnitude = 2.7 or larger, at depths of approximately 13-14 km. While the Nacimiento-Gallina area has been seismically active for a number of years, the events of 12 July are the largest events recorded to date in this region by LASN.
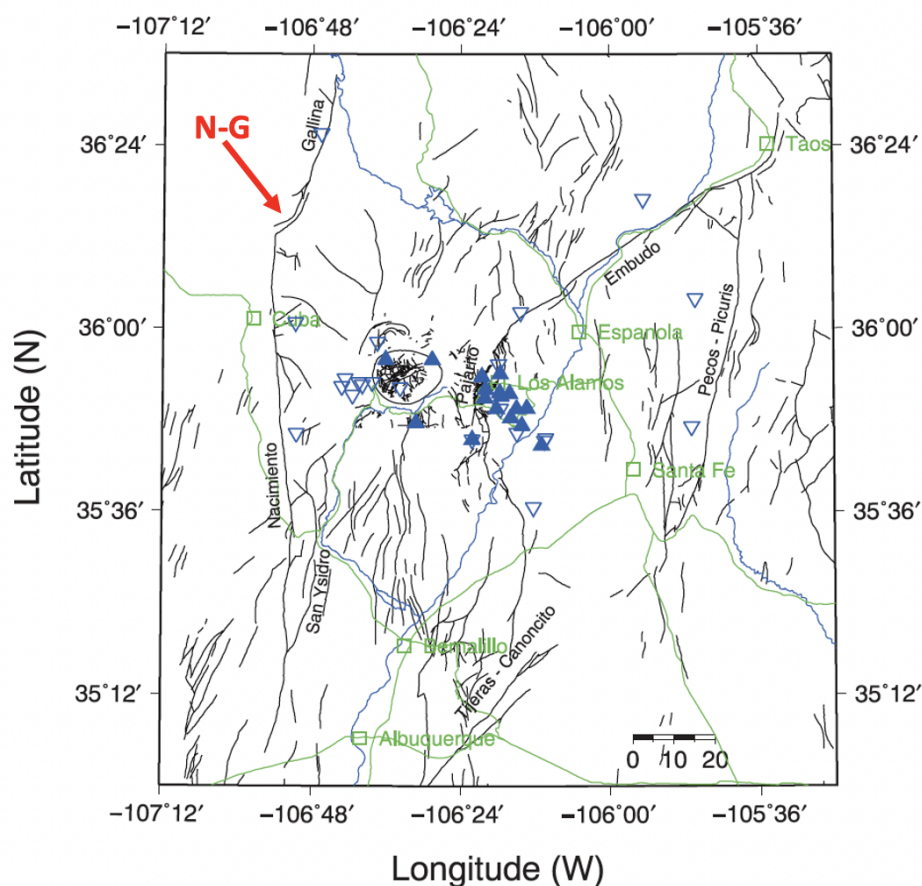
Figure 7. Map of regional faults (black lines) in northern New Mexico. Currently operating stations of the Los Alamos Seismic Network (LASN) shown as upright blue filled triangles; former LASN station locations shown as inverted unfilled blue triangles. Location of Los Alamos and other major cities in northern New Mexico labeled in green. The Nacimiento-Gallina fault junction (N-G), location of the 12 July 2021 earthquake swarm, is shown by the red arrow. Modified from [7].

While LARSA's deployment focused on capturing the anthropogenic ground-based and airborne source signatures from vehicles, this serendipitous deployment date allowed LARSA to also capture robust signatures from a nearby natural earthquake (Figure 8).
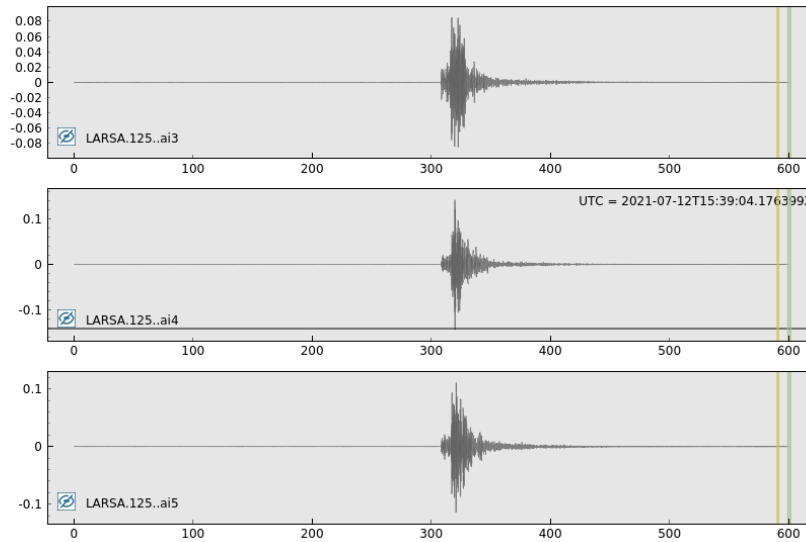
Figure 8. *Plots showing the seismic signal of the earthquake near Gallina, NM that was picked up by the deployed LARSA sensors on 12 July 2021. Plots show the vertical component (top), North/South component (middle), and the East/West component (bottom) of the seismic motion.*

## 5. Data Analyses

a. Aerial flight control data

The Gryphon Aether X8 coaxial quadcopter deployed for this mission uses a DJI A3 flight controller to communicate with the operator handset, and serve as the internal computer system. Because the flight controllers act to regulate motor speed, GPS location, and input commands, metadata of all connected systems is stored at a sub-second rate. In order to have a known UAV location in real time to compare to estimated LARSA locations for the UAV, down sampling and exporting this data was necessary. This was something the team had never previously exercised or executed for other R&D missions.

Due to proprietary locks on DJI systems, these data are not immediately useful without post-processing, and direct interface with the manufacturer for assistance with data acquisition was not a viable pathway for this project. Via an exploration of Python scripts (DROP.Py) and software, the programs DATCON and CSVView were identified as the best ways to read these files (https://datfile.net/). DATCON takes the raw .DAT file format taken directly from the flight controller and matches the internal "tick" time stamps to real time GPS time and date. This simple correction moves the internal data to a real time format, allowing for critical connections to and comparisons with other GPS-timestamped datasets, such as the seismoacoustic records recorded by LARSA. DATCON also preserves all metadata, as opposed to Python scripts which eliminate many of the time- and location-related datasets. Finally, DATCON allows for a reduction of the sample rate from up to 100 samples per second to one sample per second, reducing the overall data burden for analysis.

CSVView (https://datfile.net/) is another open-source software used to examine the CSV files generated by DATCON. This can be completed in other software (Esri ArcMap/ArcPro, Microsoft Excel) but, CSVView allows for the generating graphs and 3d spatial plots of data simultaneously, allowing for more immediate analyses of the data. This also allowed for the deletion of data points from times when the UAV was on the ground powered, but without the propellers spinning. This reduced file size and dataset volume to 1/10th of their original sizes and made comparison with LARSA data possible. The final UAV metadata were input into Esri ArcPro (https://www.esri.com/en-us/arcgis/products/arcgis-pro/overview) to provide final location and GPS-timestamped data for each flown mission.

b. Seismoacoustic data analyses of aerial targets

The processing of the array data was done using the infrapy array processing tool (see Figure 9) developed by the seismo-acoustic team in EES-17 (https://github.com/LANL-Seismoacoustics/infrapy). Infrapy is a python library capable of waveform analysis, beamforming, and source location and association analysis. It was built specifically for analyzing the infrasonic signals from large explosions, however the algorithms extend to any acoustic or seismic array analysis with simple tweaks to the frequencies and sound speeds involved.
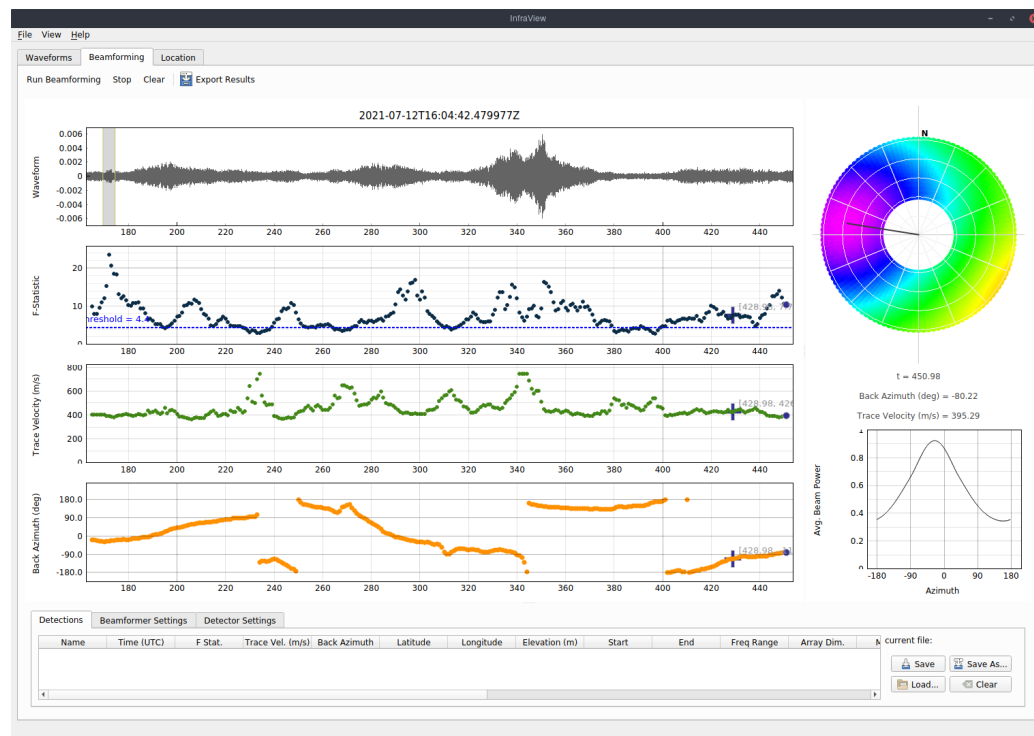
Figure 9. *Screenshot of Infraview, the graphical frontend for infrapy. Infrapy is a python library developed at LANL which is capable of acoustic waveform analysis, beamforming, and source location and association analysis. This image is of the beamforming window with plots showing (from the top): the waveform being analyzed, F-statistics, Trace velocities, and (bottom) the back azimuths for one of the UAV flights.*

The first step in the analysis was to examine the power spectra of various drone flights to determine the frequency range of the acoustic signals created by the UAV. This was done by studying the Power Spectral Density (PSD) of signals measured by the microphones in the array. An example of one of these PSDs is shown in Figure 10. Here you can see that the dominant frequency of the UAV's sound is approximately 180 Hz. This frequency will change depending on the UAV's speed and acceleration. It was determined that the best range of frequencies to track using the beamformer would be from 120 Hz to 240 Hz.
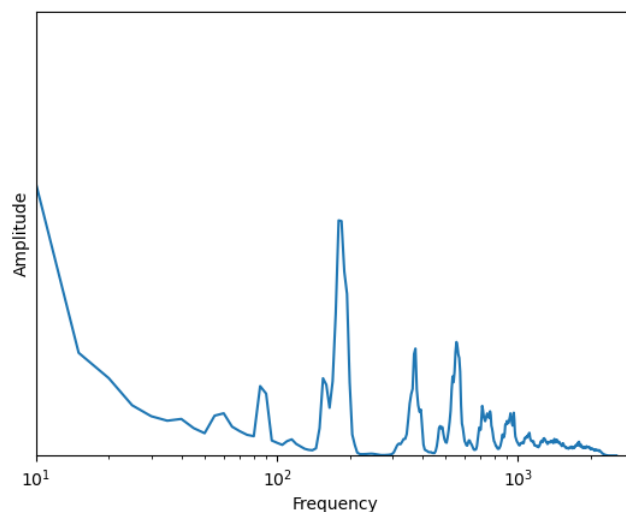
Figure 10. Plot showing an example of the Power Spectral Density of the acoustic signal created by the UAV. The large peak at approximately 180 Hz is the dominant frequency of the UAV and was used to determine that the frequency range used by the beamformer should range from 120 Hz to 240 Hz.

The beamformer (in this case a standard Bartlett beamformer) examines the signals recorded by the three microphones in the chosen frequency range, and then determines the time difference of arrivals between them as the acoustic waves pass over. Using the time delays, an approximation of the likely direction to the source that created the signal can be obtained. By breaking the signals up into 1 second increments, this process can be repeated and the position of a moving source can be tracked with good resolution and accuracy.

Figure 11 illustrates the developed passive tracking capability. In this movie, the black points are the actual location of the UAV projected to a latitude and longitude plane. The red points are the position of the UAV as provided from its onboard GPS. The green point is the location of the acoustic array, and the blue line is the back azimuth calculated with the beamforming algorithms. Full videos can be found here.
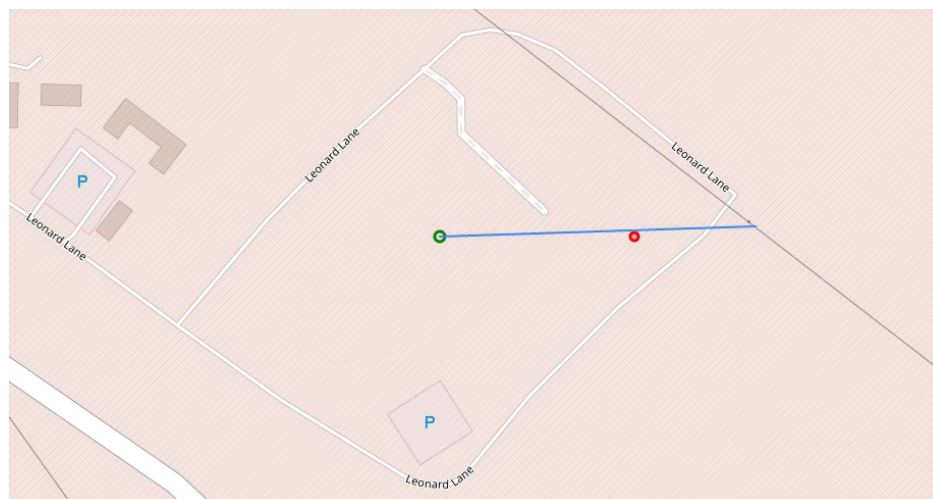
Figure 11. *Example of the UAV (red) and the back azimuth calculated by the beamforming algorithm (blue line) from the mini acoustic array (green).*

c. Seismoacoustic data analysis of ground targets

The seismic sensor network recorded signatures of ground vehicles that can be distinguished from background noise from other sources. These other sources include ground-based vehicles driving on nearby roads and aerial vehicles that were not of interest. The seismic data also included electromagnetic (EM) interference that manifested itself as discrete, sharp pulses roughly every ~0.16s (Figure 12) and thereby appear as horizontal "stripes" in our spectrogram images.

We considered these narrowband data features and restricted our analyses to the time periods when four vehicle types were driven on well-defined tracks. Ground truth vehicle positions were established through non-uniform GPS time stamps and compared to the approximate locations from analyzing the seismic data (Figure 13).
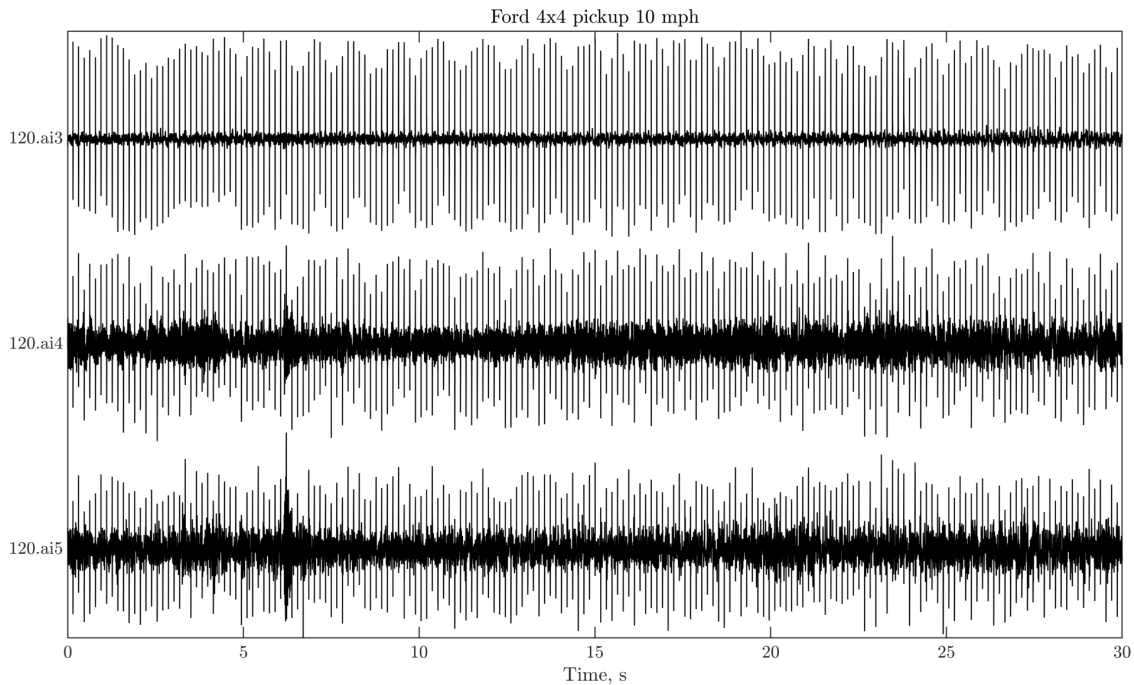
Figure 12. Seismograms on station 120 deployed near the parking location of the ground based vehicles (see Figure 3) record mechanical emissions (such as the 4x4 Ford pickup traveling at 10mph) and electrical interference that manifests as sharp spike features that give the data the "comb" like appearance. Channel ai3 measures vertical ground velocity, ai4 measures northward ground velocity, and ai5 measures eastward ground velocity. The vertical axis indicates normalized velocity, and the horizontal axis indicates time.

We investigated several methods to identify either transient or emergent signatures of ground-vehicles traffic. Initially, we found that a polarization analysis did not perform well; this method estimates source azimuths from the eigenvectors of covariance matrices computed from seismic ground motion. We attribute this relatively poor performance to the EM interference, whose harmonics left residual energy in the spectrogram data, even post-filtering. We therefore chose to normalize our data with signal energy summed over contaminated frequencies to equally weight time series samples that did include such interference. This process, while very simple, did reveal that sensors recorded peak energy over a broad time when a ground vehicle showed its point of closest approach (POCA). Figure 14 displays an example that uses station 124 (deployment relative to GPS waypoints in Figure 13) to illustrate the spectral peaks sourced by a small Toyota car.
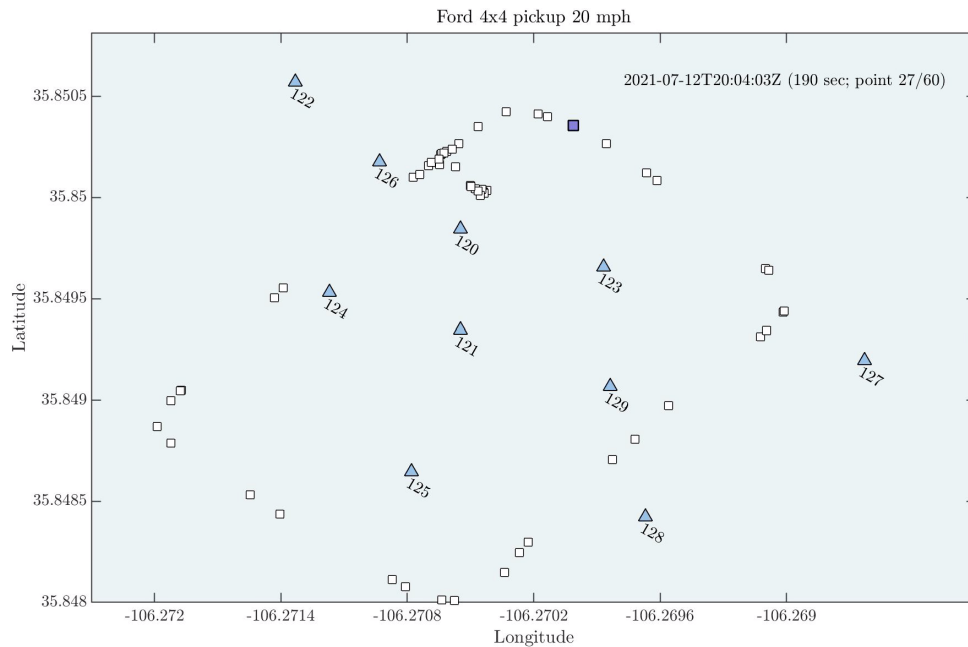
Figure 13. *Ground-based vehicle tracking methods included seismic, acoustic and GPS data (frame of movie here is shown above) that were used to develop ground truth. The purple square denotes the current location of the Ford 4x4 pickup moving up to 20mph 190s after the experiment began, at the 27th of 60 total location points. Triangles denote three channel seismometers, and small squares indicate the 60 GPS position reporting points.*
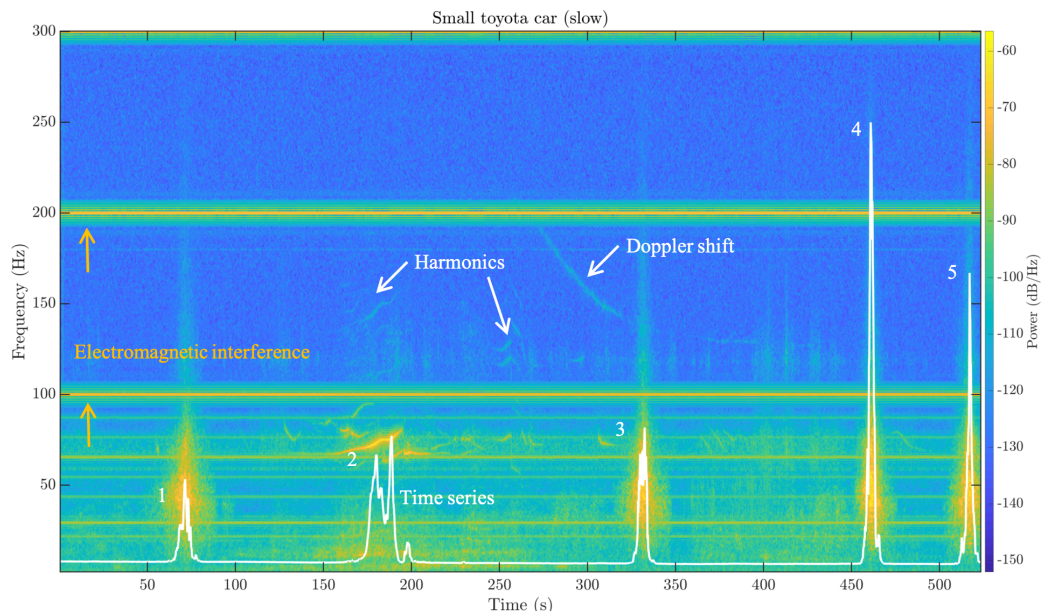
Figure 14. *A spectrogram computed at station 124 that displays the broadband spectral energy of a small Toyota car traveling less than 15 mph. The superimposed time series shows the spectral energy statistic that we normalized such that the peak time series value (at f = 250Hz) corresponds to a true value of 3.8×10^{-6} dB/Hz. Horizontal stripes in the spectrum indicate electromagnetic interference from an unknown source that was not present within the acoustic data. Text labels several features that include interference, Doppler shift, and harmonics, possibly*

from the car itself, or other road traffic. The numbers enumerate distinct peaks that associate with the POCA of the car to the sensor that associate with our animation of car traffic (animations illustrated [here](#) and [here](#)).

We integrated the frequency data to summarize the spectrograms with a one-dimensional time series (which peaked for broadband sources), then detected peaks in the time series with an energy (STA/LTA) detector. The times at these detections provided an estimate of the time of the vehicle's POCA to a sensor. We then associated peak detections across our network to the same source, under reasonable assumptions on vehicle speed (e.g., a car travels more than 0mph and less than 100mph) to form events. This effort demonstrated that such simple analyses could detect transient, broadband spectral energy and discriminate between vehicles at ~11mph versus ~18mph driving speeds (Figure 15 displays an example with a Ford pickup). While this binary detection does not uniquely identify each vehicle, it does characterize one of its operational parameters.

Multiple sensor data comparisons between GPS waypoints and integrated seismic and acoustic spectral energy additionally suggest that coincident energy peaks in both our seismic and acoustic data record vehicle acceleration. Therefore, waveform energy peaks are not uniquely sourced by vehicle proximity, but are also explained by changes in vehicle direction and speed. Features in our integrated seismic energy absent from our integrated acoustic energy estimates indicate that if a vehicles' proximity to a sensor remained fixed over time, the seismic noise at that station remained elevated (Figure 16). This elevated seismic noise energy is also attenuated quickly with sensor to vehicle distance, and such step-like changes in vehicle distance may provide a useful metric for estimating ground vehicle proximity to a sensor, when acceleration is largely absent.

Among our sensors, our processing demonstrates that Station 124 provided the clearest vehicle signatures and remained crucial for our analyses. We therefore performed a cursory analysis of the temporal coincidence of the seismic and acoustic data at station 124. This comparison demonstrates that the square-root of the product of the seismic and acoustic integrated energy localizes when the vehicle is at its POCA to the sensor.
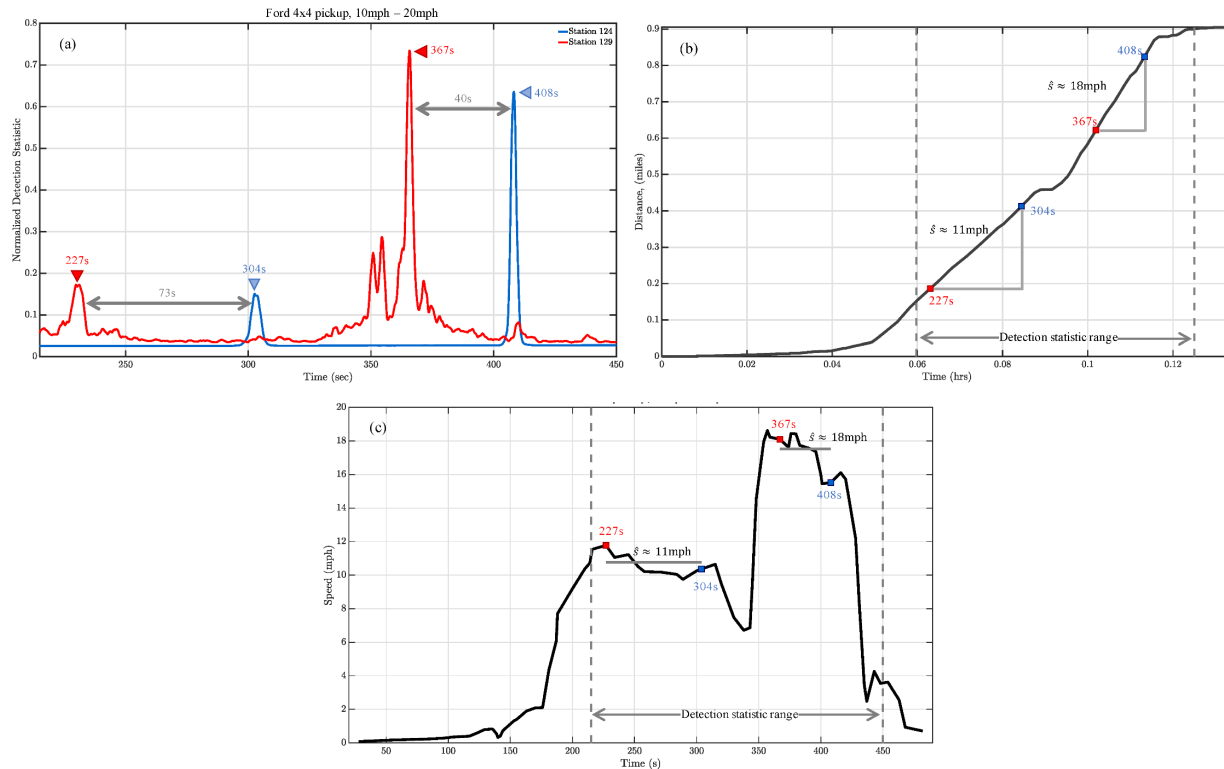
Figure 15: *Seismic analysis summary to detect and estimate the speed of a Ford 4x4 pickup truck (hereon called "pickup") using seismic sensors. This example shows records from stations 124 and 129 among 10 available sensors, over a truncated time duration. (**a**) The normalized sum of the post-processed spectral energy along three orthogonal components of motion, for each station. Markers indicate time series peaks at vehicle POCA to each respective sensor, and arrows indicate their temporal separation. (**b**) The black curve shows the distance the pickup traveled during this particular experiment as miles (vertical axis) versus time in hours (horizontal axis). The markers are associated with the detection times in (a). The solid gray horizontal and vertical lines show measurements of secant line slope and provide two estimates for the vehicle speed between each pair of detection markers, $\hat{s} = 11mph$ and $\hat{s} = 18mph$; dashed vertical lines mark the time axis limits in (a). (**c**) The thick curve shows the ground truth speed (vertical) of the pickup versus recording time (horizontal axis). Red and blue markers show detection times interpolated onto the curve. The horizontal solid gray curves show the estimates of pickup speed from (b) over the temporal duration between detections. We note that the speed estimates are consistent with the speed of the pickup in each interval. The dashed vertical lines mark the time axis limits in (a).*
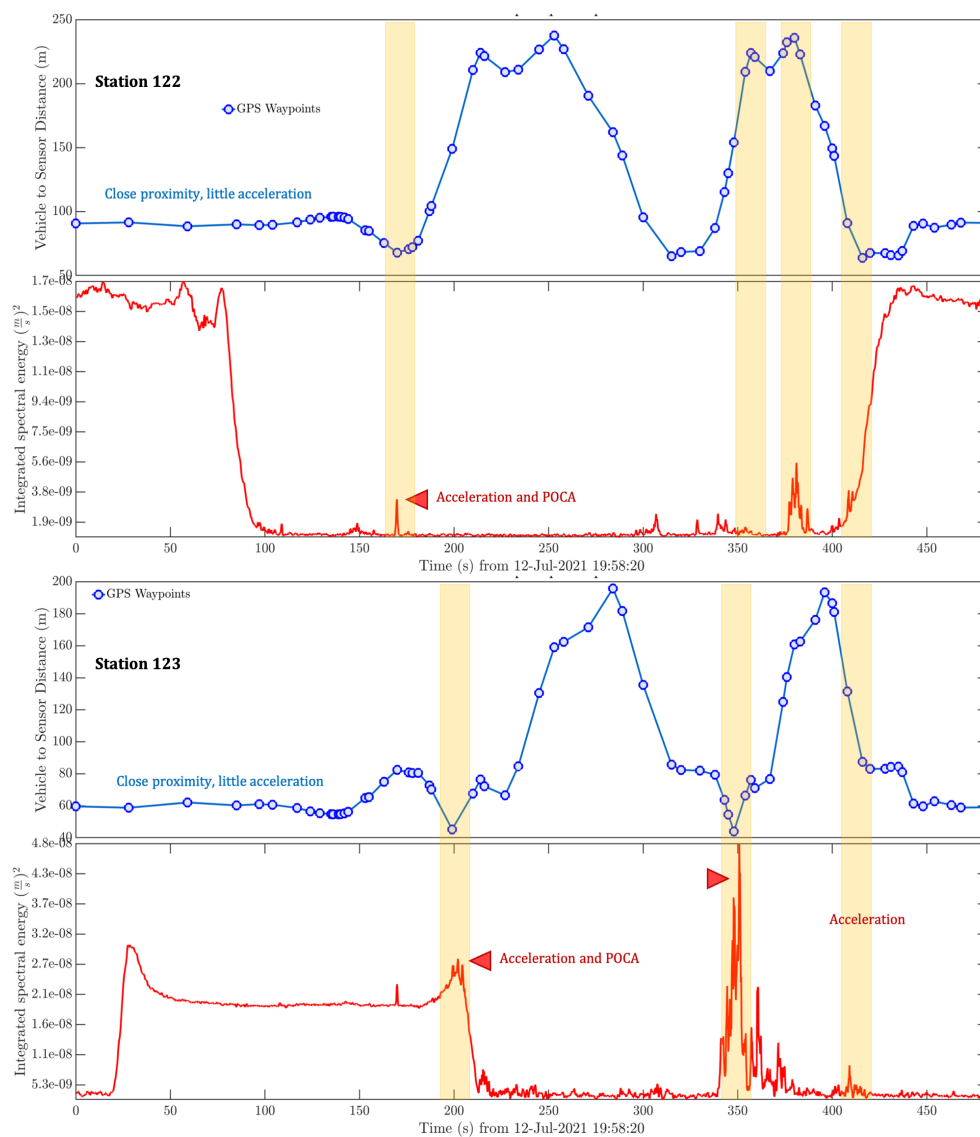
Figure 16: *Examples of integrated seismic spectral energy over time, compared against the distance of a vehicle from station 122 and 123. Mean energy levels are clearly elevated during periods that the source (a Ford 4x4 pickup truck) remains in close proximity to each sensor with limited acceleration. Conversely, acceleration events marked by highlighted bands show local maximum in recorded energy.*
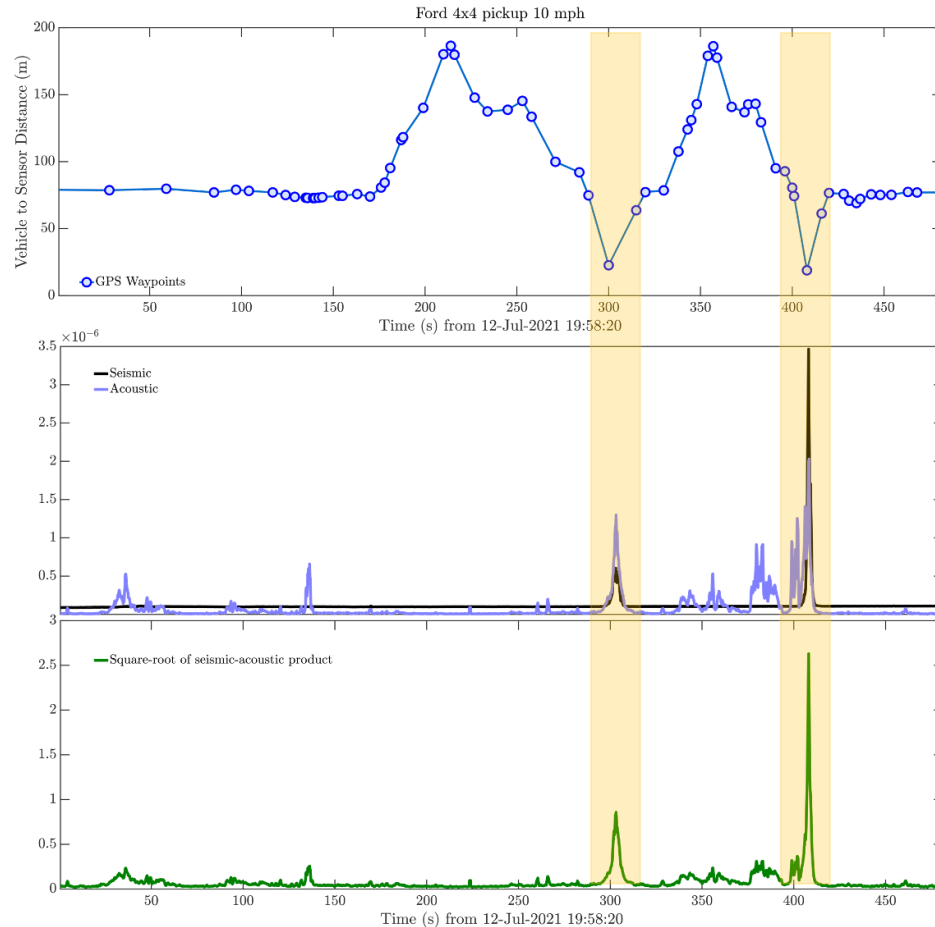
Figure 17. *A summary of seismic and acoustic signature integrated energy records for sensor 124 that recorded a Ford 4x4 pickup traveling up to 10mph around the track shown in Figure 13. The top plot illustrates the distance of the truck from sensor 124. The middle plot superimposes the integrated three channel seismic energy (black) with the acoustic energy (purple), and shows their coincidence when the truck is at the POCA to sensor 124. The bottom plot shows the square-root of the product of the seismic and acoustic energy (hybrid normalized units not shown on the vertical axis) as a green time series. The yellow highlighted regions indicate that the seismic and acoustic product mutes where the seismic and acoustic data are not temporally coincident, and demonstrates where the sources produce temporally coincident signatures at the POCA.*

d. Statistical Analyses and Forecasting

A dynamic linear model (DLM), a specific case of a state space model, is a highly flexible statistical model for time series analysis that allows relationships to vary over time. It consists of two components: (1) an observation equation that specifies how the observed measurements relate to an unobserved latent state and (2) a state equation that models how the state changes over time. Both equations incorporate uncertainty, as both the measurements and state evolution are distorted by noise. The two equations, together with a prior distribution on the initial state, completely specifies the model [8]. Once specified, the Kalman filter can be used to update the

21

inference on the state as new data becomes available, which in turns allows for prediction of the observations through the observation equation, e.g., tracking a moving object between successive time points [9].

The work of [10] adopts the Kalman filter approach to a track-while-scanning operation. It assumes the measurements are the range and bearing from a radar sensor, but predicts the Cartesian coordinate location of an object through conversion from polar coordinates. The state vector consists of the location of the object as well as the velocity in two directions and also includes a parameter for the acceleration of the object. The Kalman filter approach has been extended to the 3-dimensional case where elevation angle is incorporated, in addition to range and bearing. This 3-dimensional extension creates nonlinearity in the observation equations and modifications must be made to the simple Kalman filter estimation formulation [11,12]. Although not demonstrated here, extending the Kalman filter to forecasting UAV elevation (AGL) is part of future work.

Applying the track-while-scanning Kalman filter method assumes that the data is in the form of range, r, and bearing, θ. The beamformer approach of Section 5b, produces a back azimuth from the acoustic signal, which can be used as θ. To obtain values for r, the GPS data collected from the drone can be used with a simple conversion. The GPS data can also be used as an alternative method to inputting the position bearing.

The results in Figures 18 and 19 show the one-step ahead prediction, as the mean of the posterior distribution from the Kalman filter for mission 1 (the top plot of Figure 11). The first plot shows the prediction when the bearing is estimated from the GPS coordinates. For a portion of the time steps the one-step ahead prediction aligns with the true location of the UAV. However, the code fails to predict any locations to the left of the sensor location (indicated by the red dot in the center of the plot). Understanding why this phenomenon is occurring is a part of future research. The predictions in the second plot are not more accurate and indicate an implausible drone path that jumps around the scene. Again, understanding why the algorithm does not predict a smoother path is an area of opportunity for this work. Figures 18 and 19 are displayed as GIFs where ten one-step ahead predictions are added at a time and can be viewed here.
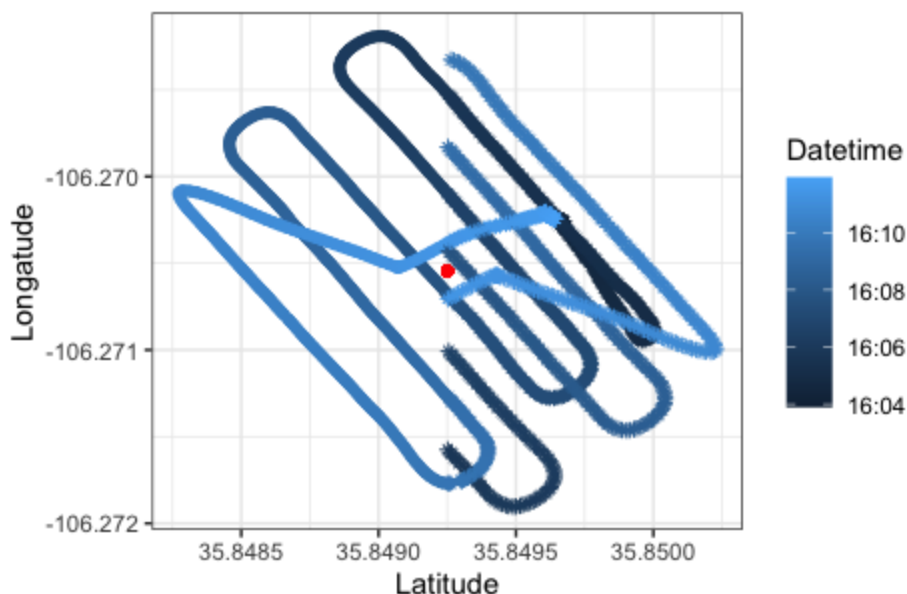
Figure 18. *Prediction of UAV location using the GPS from the UAV flight controller to compute the range and bearing. The filled in circles are the ground truth, the stars are the predicted values, and color corresponds to the time, so points go from dark to light as time passes. There is a corresponding ground truth and prediction for each color. The methodology does not predict to the left of the sensor (red dot).*
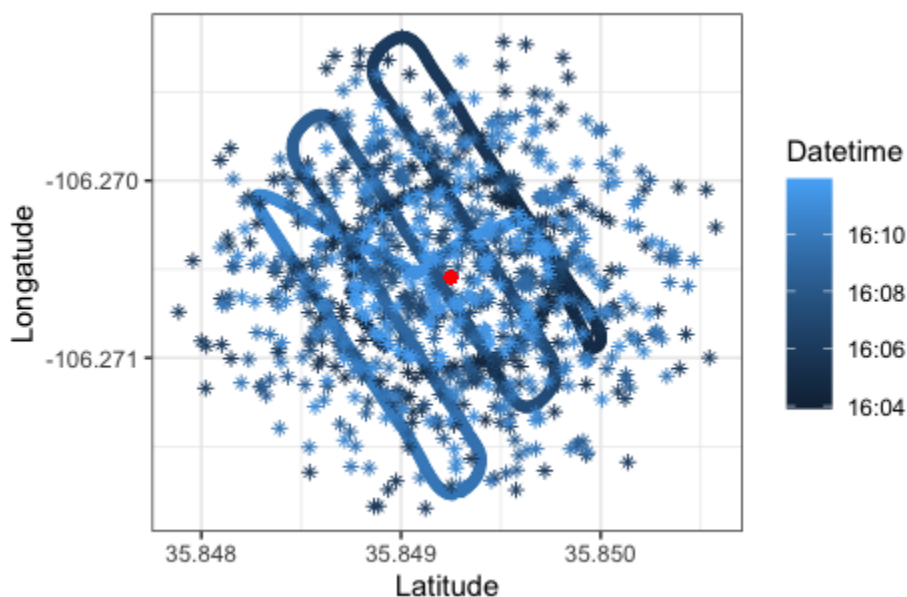
Figure 19. *Prediction of UAV location using the GPS from the UAV flight controller to compute the range and the computed back azimuth for the bearing. The filled in circles are the ground truth, the stars are the predicted values, and color corresponds to the time, so points go from dark to light as time passes. There is a corresponding ground truth and prediction for each color. There is no discernible pattern.*

Figure 20 compares the estimated bearing from the UAV GPS signal to the back azimuth computed with the beamformer approach of Section 5b, where each point represents the estimated θ at a particular point in time. The linear section in the middle of the plot indicates that the predictions from both methods follow a similar pattern; however, the areas to the left and right of the linear section indicate a shift in one or both estimation methods. Again, this discrepancy provides an opportunity to learn more about the Kalman filter approach and how best to replicate a track-while-scan operation with acoustic measurements.
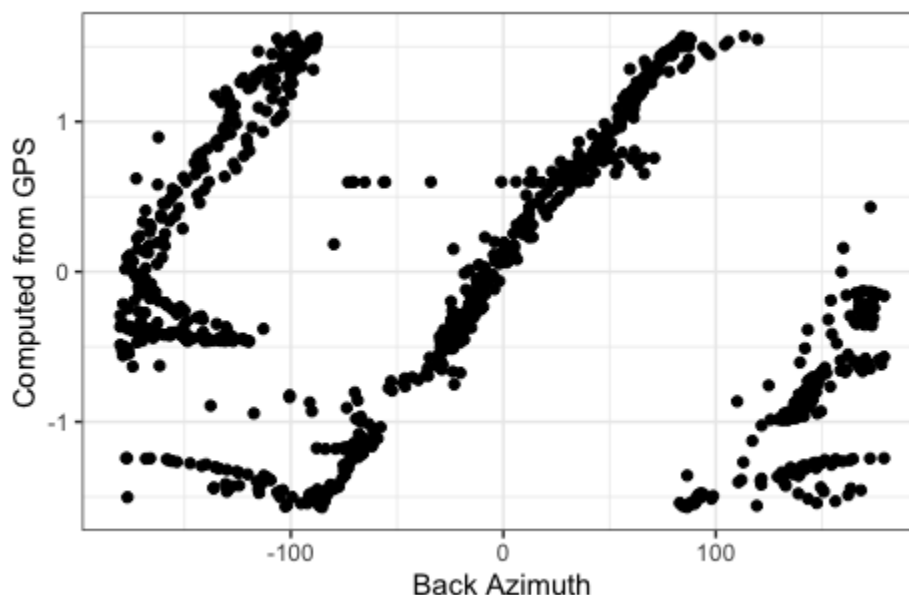
Figure 20. *Comparison of the bearings when computed from the back azimuth (x-axis) to that computed from the GPS location (y-axis). Each point represents one point in time.*

6. Discussion and Conclusions
A. Experiment Design and Execution
We demonstrated the ability to design a relevant and applicable field campaign at a local LANL site, and execute the sensor and source deployments effectively and efficiently. As the team expands its UAV fleet, future studies could test detection and discrimination of multiple UAVs in flight, and evaluate potential for detection of multiple airborne targets. Future work could also be performed against other sites of interest, including explosives testing sites where a wider variety of large ground vehicles are in use. Additionally, conducting additional data collections at testbeds with increased background noise would help to identify the signal-to-noise thresholds of the LARSA sensors in detecting signals of UAVs and specific vehicle types in heavy industrial and civil infrastructure areas.

B. Statistical Analysis for Sensor Deployment Optimization
We demonstrated the ability to determine sensor location to specifically address a question of interest using the expected signal from a particular modality. For this work,

we used the acoustic signal to directly localize the UAV at all points in the UAV's flight with an increased emphasis on the locations where the acoustic signal is likely to be more prevalent, i.e., the take-off and landing location and the turns along the flight path. This approach assumed a constant acoustic velocity and therefore optimization occurred with respect to the distance. This approach differs from previous sensor deployment optimizations because the source is moving and thus sensor placement must be optimized while also integrating over the entire expected path. In addition, a space filling approach was also employed to ensure the area of operation was sufficiently covered.

An important methodological development that could be addressed with the data collected in this study is how to optimize sensor deployment with multiple modalities. The deployment scenario considered only acoustic signals, but a model could be built with the collected seismic and acoustic data to predict the expected signal at multiple locations, and a joint optimization for both modalities could be conducted. Future studies could be conducted in areas of more challenging terrain to more comprehensively evaluate the role played and sensitivity imparted by topography in this study's sensor deployment optimization. In addition, this data could be used to address the question of how many sensors is enough for (1) detection and (2) path forecasting?

C. Acoustic detection and screening of airborne vehicles

We demonstrated that an acoustic array can provide valuable and accurate tracking information for airborne vehicles. Traditional beamforming techniques were able to track the UAV as it moved through the P-J plot and were capable of providing accurate back azimuth information at distances approaching 100 meters. The algorithm used assumes a single target so at points the tracking left the UAV and seemed to track vehicles passing by on the nearby Pajarito Road corridor. Future work would include multiple arrays with higher numbers of elements, as well as the use of more complex algorithms to separate multiple targets, or to better separate targets from background noise.

D. Seismoacoustic detection and screening of ground based vehicles

We demonstrated an ability to use a seismic network of three channel seismometers to detect the point of closest approach of ground-based vehicles (Figure 14) and estimate their average speeds. The strength of the signal from the sensor data was variable across the network; in particular, certain stations (124) provided much better records of vehicle traffic than others (e.g., 128). In addition, our high frequency sensors were contaminated with electromagnetic interference (Figure 13) that challenged polarization analysis that could better track the direction of arrival of these vehicles; however, understanding how to adapt this methodology to cope with the interference is an opportunity for future work. Our data also reveal other features that include Doppler shift below 300Hz from variable sources, and their harmonics. We did not attempt to identify these energy sources. Importantly, we can identify passenger vehicles among these various energy sources and amongst interference, categorize such vehicles by speed (Figure 15), and count the number of times they pass each sensor on the track. We

conclude that we can calculate basic traffic parameters from three channel seismic data, using routine processing methods, and that these estimates agree well with ground truth derived from GPS data.

7. **Impacts**

Detecting, identifying and tracking a target with active interrogation (e.g. radar) is a well-established technology - both in terms of sensing technology and algorithms. However, active interrogation always provides a signal that can be used to locate the interrogator system. Single targets can generate a signal that might be observed passively. These signals include electromagnetic signals from an engine/motor, chemical/gas signatures and mechanical waves. Electromagnetic signals are often embedded into complex background noise signals, and while chemical/gas signals provide invaluable information, attributing these signals to a target can be difficult due to complex propagation paths. Propagation of seismic and acoustic waves, observed within approximately 200 kilometers between target and interrogator, is not as complicated. These mechanical waves can be guided by geology and topography, however if the path between a target and interrogator is direct and somewhat homogeneous, then such signals might be exploited to form a passive interrogation tracking system. In this project, we have demonstrated, at a small scale, the viability of such a system for a single isolated target. Algorithms and associated sensing systems for passive detection/identification/tracking are relevant to diverse national security and military missions, law enforcement, and facility protection. Needed seismic and acoustic sensors are inexpensive and with the development of mature algorithms, a passive seismo-acoustic tracking system could provide a cost-effective option for target detection, identification and tracking.

ACRONYMS AND DEFINITIONS

3-D	three-dimensional
AGL	above ground level
CCS	Computer, Computational, and Statistical Sciences Division
CSV	comma-separated values
dB	decibel
DoE	Design of Experiment
DDSTE	Deputy Directorate for Science, Technology, and Engineering
DLM	dynamic linear model
EES	Earth and Environmental Sciences Division
EM	electromagnetic
FAA	Federal Aviation Administration
GIF	graphics interchange format
GPS	Global positioning system
GS-NSD	Global Security – National Security and Defense Program Office
GS-PROG	Global Security Program Office
Hz	Hertz
INT	Intelligence
kg	kilogram
kHz	kilohertz
LANL	Los Alamos National Laboratory
LARSA	Los Alamos Rapid-Deployable Seismoacoustic Array
LASN	Los Alamos Seismic Network
LIDAR	light detection and ranging
mAh	milliamp hours
mph	miles per hour
m/s	meters per second
NM	New Mexico
P-J	TA-51 Pinon-Juniper Plot
POCA	point of closest approach
PSD	power spectral density
SEC-DO	Security Division
STA/LTA	short-term averaging/long-term averaging
SUV	sport utility vehicle
TA-51	Technical Area 51
TVS	Time-varying signatures
UAS	Uncrewed aerial system; an aircraft plus one or more payload components
UAV	Uncrewed aerial vehicle; aircraft only
UTV	Utility task vehicle

REFERENCES

[1] Weaver, B. P., Williams, B. J., Anderson-Cook, C. M., & Higdon, D. M. (2016). Computational enhancements to Bayesian design of experiments using Gaussian processes. *Bayesian Analysis*, 11(1), 191-213.

[2] Michaud, I. J. (2019). Simulation-Based Bayesian Experimental Design Using Mutual Information (Doctoral dissertation, North Carolina State University).

[3] Williams, Brian. (2020) "Bayesian Optimal Sensor Augmentation Via Estimated Mutual Information" LA-UR-20-27616.

[4] Schultz-Fellenz, E.S., Coppersmith, R.T., Sussman, A.J., Swanson E.M., Cooley J.A. (2018). Detecting Surface Changes from an Underground Explosion in Granite Using Unmanned Aerial System Photogrammetry. *Pure and Applied Geophysics* 175, 3159–3177. https://doi.org/10.1007/s00024-017-1649-0.

[5] Schultz-Fellenz, E.S., Swanson, E.M., Sussman, A.J., Coppersmith, R.T., Kelley, R.E., Miller, E.D., Crawford, B.M., Lavadie-Bulnes, A.F., Cooley, J.A., Vigil, S.R., Townsend, M.J., Larotonda, J.M. (2020). High-resolution surface topographic change analyses to characterize a series of underground explosions. *Remote Sensing of Environment* 246, https://doi.org/10.1016/j.rse.2020.111871.

[6] Crawford, B., Swanson, E., Schultz-Fellenz, E., Collins, A., Dann, J., Lathrop, E., Milazzo, D. (2021). A New Method for High Resolution Surface Change Detection: Data Collection and Validation of Measurements from UAS at the Nevada National Security Site, Nevada, USA. *Drones*, 5(25). https://doi.org/10.3390/drones5020025.

[7] House, L., and Roberts P. (2020). Seismicity monitoring in north-central New Mexico by the Los Alamos Seismic Network. *Seismological Research Letters*, 91(2A), 593-600.

[8] Casleton, E., Osthus, D., & Van Buren, K. (2018). Imputation for multisource data with comparison and assessment techniques. *Applied Stochastic Models in Business and Industry,* 34(1), 44-60.

[9] Petris, G. (2010). An R package for dynamic linear models. *Journal of Statistical Software*, 36(1), 1-16.

[10] Castella, F. R., & Dunnebacke, F. G. (1974). Analytical results for the x, y Kalman tracking filter. *IEEE Transactions on Aerospace and Electronic Systems*, (6), 891-895.

[11] Park, S. T., & Lee, J. G. (2001). Improved Kalman filter design for three-dimensional radar tracking. *IEEE Transactions on Aerospace and Electronic Systems*, 37(2), 727-739.

[12] Raj, K. D. S., & Krishna, I. M. (2015, February). Kalman filter based target tracking for track while scan data processing. In: 2015 2nd International Conference on Electronics and Communication Systems (ICECS) (pp. 878-883). IEEE.